In situ evaluation of spaceborne CALIOP lidar measurements of the upper-ocean particle backscattering coefficient

Léo Lacour, Raphael Larouche, Marcel Babin

Research Article | Vol. 28, No. 18 / 31 August 2020 / Optics Express 26989
Optics EXPRESS

In situ evaluation of spaceborne CALIOP lidar measurements of the upper-ocean particle backscattering coefficient

LÉO LACOUR,* RAPHAEL LAROUCHE, AND MARCEL BABIN

UMI Takuvik, CNRS/Université Laval, Québec, QC, Canada
leo.lacour@takuvik.ulaval.ca

Abstract: The spaceborne CALIOP lidar, initially designed for atmospheric measurements, was recently used to retrieve the particulate backscattering coefficient (b_{bp}) in ocean subsurface layers. However, extensive field evaluation of CALIOP estimates was never conducted due to the scarcity of in situ data. Here, year-round and basin-wide data from Biogeochemical Argo floats (BGC Argo) were used to evaluate CALIOP estimates in the North Atlantic. The high density of BGC Argo float profiles in this region allowed us to test different matchup strategies at different spatio-temporal scales. When averaged over 2° by 2° grid boxes and monthly time resolution, CALIOP data present reasonably good correlation with highly variable float b_{bp} values (correlation $r = 0.44$, root mean square relative error $RMS\% = 13.2\%$), suggesting that seasonal dynamics can be characterized at basin scale.

1. Introduction

The National Aeronautics and Space Administration (NASA) and the Centre National d'Etudes Spatiales launched in 2006 the Cloud-Aerosol Lidar and Infrared Pathfinder Satellite Observation (CALIPSO) satellite [1]. The primary instrument on CALIPSO is the Cloud-Aerosol Lidar with Orthogonal Polarization (CALIOP) sensor, initially designed for atmospheric studies [2]. However, recent studies have demonstrated the potential of CALIOP for oceanic applications [3–6]. CALIOP subsurface measurements provide estimates of the backscattering coefficient of suspended particles ($b_{bp}(\lambda)$, m^{-1}) from which phytoplankton biomass or particulate organic carbon can be derived [3]. These active lidar measurements can be conducted both day and night, at low solar elevations and through considerable aerosol loads and thin clouds, thus palliating many limitations of passive ocean color remote sensing, particularly in polar and subpolar regions [7,8].

Field evaluation of satellite observations has always been a challenging issue in oceanographic research. Indeed, field-collected data are sparse in time and terribly undersampled in space [9], thus restricting matchups of data to specific locations and times. To our knowledge, only one study from Behrenfeld et al. [3] conducted a comparison analysis between CALIOP subsurface b_{bp} retrievals and in situ data. They used ship-based b_{bp} data collected during the 2012 AMT22 cruise in the North Atlantic between 15 (45°N, 20°W) and 24 October (22°N, 40°W). These data were compared with nearest 2° by 2° pixels of monthly climatological average CALIOP b_{bp} data, and 9 by 9 km pixels of monthly average MODIS b_{bp} data for October 2012. Therefore, differences in spatial and temporal resolutions of b_{bp} data from the various sources induced discrepancies in matchups. In addition, the CALIOP b_{bp} data could not be evaluated over the full seasonal cycle.

The recent deployments of profiling Biogeochemical Argo floats (BGC-Argo) in the North Atlantic subpolar ocean provide the first opportunity to evaluate CALIOP b_{bp} estimates with year-round and basin-wide in situ b_{bp} data. The density of the BGC-Argo float network allowed us to test different matchup configurations at different spatio-temporal scales. In particular,

#397126 https://doi.org/10.1364/OE.397126
Journal © 2020 Received 8 May 2020; revised 1 Aug 2020; accepted 3 Aug 2020; published 28 Aug 2020

Optics EXPRESS

matchups on a profile-by-profile basis were conducted to evaluate if CALIOP estimates may be used at fine spatio-temporal scales to better describe phytoplankton blooms dynamics in polar and subpolar regions.

2. Method

2.1. Robotic in situ observations

In situ observations were acquired by an array of 18 BGC-Argo floats deployed in the North Atlantic subpolar ocean (Table 1, freely available at http://www.coriolis.eu.org/Data-Products/Data-Delivery/Data-selection). These autonomous profiling platforms, equipped with state-of-the-art biogeochemical sensors, have collected measurements every 2, 5 or 10 days, from 1000 m (drifting depth) to the surface. In 2014, more than 1000 profiles were acquired in this region, representing the highest annual density of BGC-Argo float profiles worldwide (Fig. 1). This unique profile density allowed us to test different matchup configurations, binning the data at different spatio-temporal resolutions (see section 2.4). This is why our analysis focuses on this specific region and year.

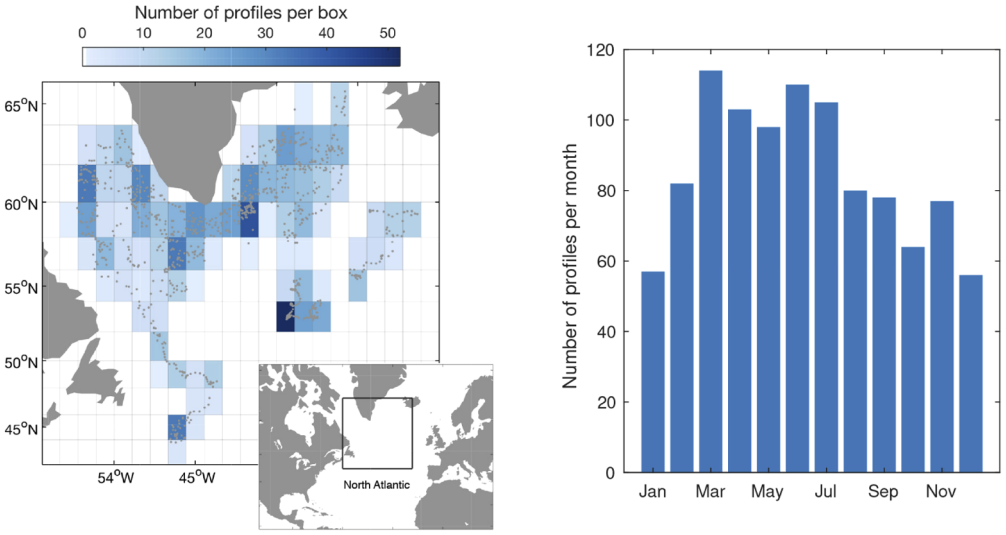

Fig. 1. Spatial distribution over 2° by 2° grid boxes (left) and temporal distribution (right) of >1000 BGC-Argo float profiles acquired in 2014 in the North Atlantic subpolar ocean.

A WETLabs ECO sensor, mounted on each float, has measured the volume scattering function (VSF) in the backward direction, at a wavelength (λ) of 700 nm and an angle of 124°. Following the procedures described in Schmechtig et al. [10], the contribution of seawater was removed from the VSF, which in turn was converted to total particle backscattering $b_{bp}(700)$ with the conversion factor from Sullivan et al. [11]. To match CALIOP estimates at 532 nm, $b_{bp}(700)$ was scaled to 532 nm according to:

$$b_{bp}(532) = b_{bp}(700)\left(\frac{700}{532}\right)^{\gamma} \quad (1)$$

where the power-law slope (γ) was set equal to 0.78 [12]. Finally, for comparison with CALIOP and MODIS estimates, $b_{bp}(532)$ was depth-averaged with the following vertical weighting

Optics EXPRESS

Table 1. List of Biogeochemical-Argo floats used in this study.

WMO[a]	# Profiles	Date first profile	Date last profile
6901486	59	07-Jan-2014	28-Dec-2014
6901489	60	07-Jan-2014	23-Dec-2014
6901516	126	04-Jan-2014	27-Dec-2014
6901480	116	04-Jan-2014	29-Dec-2014
6901484	25	05-Jan-2014	12-Apr-2014
6901485	60	05-Jan-2014	26-Dec-2014
6901481	10	05-Jan-2014	06-Mar-2014
6901482	60	05-Jan-2014	26-Dec-2014
6901524	60	05-Jan-2014	26-Dec-2014
6901525	111	05-Jan-2014	27-Dec-2014
6901515	9	06-Jan-2014	02-Mar-2014
6901519	59	06-Jan-2014	27-Dec-2014
6901517	8	06-Jan-2014	25-Feb-2014
6901521	16	06-Jan-2014	06-Apr-2014
6901523	60	06-Jan-2014	27-Dec-2014
6901527	69	06-Jan-2014	22-Dec-2014
6901647	63	09-Jun-2014	27-Dec-2014
6901646	53	16-Jun-2014	29-Dec-2014

[a]World Meteorological Organization identification number

function [13,14]:

$$b_{bp}^{FLOAT} = \frac{\sum \exp(-2K_d(532)z)\ b_{bp}(532,z)}{\sum \exp(-2K_d(532)z)} \tag{2}$$

where $K_d(532)$ is the diffuse attenuation coefficient of downwelling irradiance at 532 nm (m^{-1}). $K_d(\lambda)$ was first computed at 490 nm by fitting a fourth-degree polynomial function on the logarithm of the downwelling irradiance $E_d(490)$ measured by the floats (OCR-504, Satlantic Inc.), and then calculating the mean slope over the first 50 meters. Based on the quality-control procedure described in Organelli et al. [15], only profiles of type 1 and 2 (for "good" and "probably good") were used. In addition, each data point acquired along the profile flagged as "bad" or "probably bad" were removed. For 30% of the dataset, the quality of the profiles was too bad (type 3) to calculate $K_d(490)$. In these cases, we used the average $K_d(490)$ of profiles, within a radius of 100 km and a time period of 20 days (the decorrelation scale of bio-optical properties [16]), where b_{bp}^{FLOAT} had changed by less than 50%. $K_d(490)$ was then scaled to 532 nm according to [17]:

$$K_d(532) = 0.68\ (K_d(490) - 0.022) + 0.054 \tag{3}$$

2.2. Passive ocean color observations

Passive ocean color observations from the MODIS Aqua sensor were downloaded from https://oceancolor.gsfc.nasa.gov. Monthly and 8-day level-3 products at 9 by 9 km grid resolution were used. The particle backscattering coefficient at 443 nm ($b_{bp}(443)$) was computed using the Generalized Inherent Optical Properties inversion algorithm (GIOP) [18]. MODIS-based $b_{bp}(443)$ was converted to $b_{bp}(532)$ (hereafter b_{bp}^{MODIS}) using a formula similar to Eq. (1), with γ directly provided by the GIOP algorithm.

Optics EXPRESS

2.3. Active CALIOP measurements

The CALIOP lidar is an active sensor producing simultaneous laser pulses at 1064 and 532 nm, with dual polarization at 532 nm (cross-polarization and co-polarization channels). The beam is directed at a fixed angle near nadir, and the angular divergence is adjusted to produce a beam diameter of 70 m at the Earth's surface. The along-track pulse-to-pulse distance is 333 m and the between-track distance is 1.5° at the equator (decreasing with increasing latitudes). CALIOP orbit has a 16-day repeat cycle, during which world-wide vertical profiles of the elastic backscattering are recorded. Fundamental profiles' vertical resolution is 30 m in the atmosphere and ~22.5 m in the water because of the 1.34 refractive index of seawater at 532 nm [19].

Level 1B Standard V4-10 CALIOP profiles from https://search.earthdata.nasa.gov/search were used to estimate the ocean particle backscattering coefficient following the methodology described in Behrenfeld et al. [3]. Briefly, CALIOP b_{bp} estimates were based on the cross-polarized component of column-integrated backscatter from below the ocean surface, β_{w+}. As signal level in the ocean changes with the transmittance of the overlying atmosphere, β_{w+} was derived from the column-integrated ratio of the co-polarized and cross-polarized channels (i.e. depolarization ratio). This ratio is independent of atmospheric transmittance and is very accurately calibrated:

$$\beta_{w+} = \delta_T \frac{\beta_s}{1 - 10\delta_T} \tag{4}$$

where δ_T is the total column-integrated depolarization ratio (dimensionless), which includes surface and subsurface signals (first vertical bin below surface). The ocean surface position was determined as the maximum total backscatter (sum of co- and cross-polarized channels) located within 150 meters above or below the reported Global 30 Arc-Second (GTOPO30) Digital Elevation Model (DEM) following Lu et al. [17]. β_s is the lidar surface backscatter (sr^{-1}), which retains the transmitted laser pulse polarization plane and impacts the co-polarized channel. β_s was evaluated using co-located ocean surface wind speed estimates from ECMWF reanalysis according to Hu et al. [20]. Then, b_{bp}^{CALIOP} at 532 nm was computed as:

$$b_{bp}^{CALIOP} = \frac{2K_d(532)\beta_{w+}}{P_p(\theta,\lambda)*0.98^2} \frac{1+\delta_p}{\delta_p} \tag{5}$$

where $P_p(\theta,\lambda)$ is the scattering phase function in the backward direction due to particles. At angle (θ) of 180° and wavelength of 532 nm, $P_p(180, 532)$ is assumed to be 0.32 following Lu et al. [21]. This value differs from the study of Behrenfeld et al. [3] where $P_p(\theta,\lambda)$ was set equal to 0.16. The reason of this choice will be discussed in section 3. δ_p is the particulate depolarization ratio in water, estimated as $\delta_p = 2K_d(532)$ for waters with $K_d(532)$<0.15 m^{-1} or $\delta_p = 0.3$ for waters with $K_d(532)$>0.15 m^{-1} [3]. Usually, $K_d(532)$ is computed from collocated MODIS observations [17,22]. Here, $K_d(532)$ was derived from float measurements (see section 2.1), allowing CALIOP b_{bp} estimates to be independent from passive satellite observations.

Two sets of Quality Check flags, contained in lidar Level 1 data products, were applied at single shot resolution to insure high-quality CALIOP retrievals. In addition, as the presence of sea ice, extreme wind conditions, clouds and high aerosol loading compromise CALIOP measurements, some quality thresholds were employed, following Behrenfeld et al. [3]. CALIOP retrievals with δ_T>0.05 were removed to eliminate measurements with complete or partial sea ice coverage within a given lidar footprint. Single-shot data under wind speeds of > 9 m s^{-1} were removed as well to avoid signal contamination from bubbles, foam, and whitecaps. Similarly, data under wind speeds of < 2 m s^{-1} were also removed to avoid potential errors from saturation of the co-polarization channel due to strong specular reflection from the ocean surface. Finally, following Lu et al. [17], lidar shots with column-integrated backscatter above the ocean surface > 0.03 sr^{-1} were removed to warrant the air column is sufficiently clear and clean. This value

Optics EXPRESS

corresponds approximately to an aerosol optical depth of 3, a threshold used in Behrenfeld et al. [3].

2.4. Evaluation strategy of CALIOP b_{bp} estimates

CALIOP b_{bp} estimates were evaluated by comparison with both in situ autonomous robotic observations from BGC-Argo floats and passive ocean color data from MODIS in 2014. The comparison zone is the North Atlantic subpolar ocean between 42° and 66° N. Comparisons between float and MODIS estimates were also conducted. The advantage of using float data is that matchup with CALIOP data were possible throughout the year, on a basin scale. The high density of the float network allowed us to test three matchup configurations: (1) Single float profiles were co-located with the nearest 9 by 9 km MODIS pixel and CALIOP shots covering the same area. Both MODIS and CALIOP data were averaged over 16-day periods, corresponding to CALIOP repeat cycle time. (2) Float, CALIOP and MODIS data were binned over 1° by 1° grid boxes and 16-day periods. (3) Boxes were extended to 2° by 2° and monthly time periods.

To evaluate the performance of CALIOP retrievals, the log-difference error (Δ) between estimates from each source was calculated, as described in Campbell et al. [23] and Friedrichs et al. [24]:

$$\Delta_{(MODIS,CALIOP)} = log_{10}(b_{bp}^{MODIS}) - log_{10}(b_{bp}^{CALIOP}) \tag{6}$$

$$\Delta_{(FLOAT,CALIOP)} = log_{10}(b_{bp}^{FLOAT}) - log_{10}(b_{bp}^{CALIOP}) \tag{7}$$

$$\Delta_{(MODIS,FLOAT)} = log_{10}(b_{bp}^{MODIS}) - log_{10}(b_{bp}^{FLOAT}) \tag{8}$$

The mean (M) and standard deviation (SD) of the log-difference errors, and root-mean-square (RMS%) of the relative log-difference errors were also examined. As an example, $M_{(MODIS,CALIOP)}$ would be the mean of $\Delta_{(MODIS,CALIOP)}$. Since these indices are expressed in decades of log and not easily translated into absolute terms, Campbell et al. [23] proposed non-dimensional inverse-transformed values:

$$F_{med} = 10^{M} \tag{9}$$

$$F_{min} = 10^{M-SD} \tag{10}$$

$$F_{min} = 10^{M-SD} \tag{11}$$

Assuming an underlying normal distribution for Δ, $F_{med}^{(MODIS,CALIOP)}$, for example, would be the median value of the ratio $F = b_{bp}^{MODIS}/b_{bp}^{CALIOP} = 10^{\Delta_{(MODIS,CALIOP)}}$. Thus, if $F_{med}^{(MODIS,CALIOP)} = 2$, the median value of b_{bp}^{MODIS} is a factor of 2 larger than the median value of b_{bp}^{CALIOP}. Similarly, if $F_{med}^{(MODIS,CALIOP)} = 0.5$, the median value of b_{bp}^{MODIS} is a factor of 2 smaller than the median value of b_{bp}^{CALIOP}. The correlation coefficient (r) was also calculated from the log-transformed values.

3. Results and discussion

The spatio-temporal coverage of BGC-Argo profiles allowed, for the first time, year-round and basin-wide in situ comparisons with CALIOP estimates. Over the whole basin, a minimum of 56 profiles were acquired in December, and a maximum of 114 profiles in March, with an average of 85 profiles per month in 2014 (Fig. 1). By contrast, the availability of passive MODIS observations was limited in winter due to low solar elevations at these latitudes. Indeed, over 2° by 2° boxes (i.e. ConFig. 3), no monthly MODIS data were available in January and < 20% of pixels in February, November and December on average (Fig. 2). Data availability was maximum in August (99% of pixels).

With CALIOP quality flags implemented (see section 2.3), b_{bp} estimates were retrieved throughout the year, but from only a small proportion of the CALIOP shots. While good-quality

Optics EXPRESS

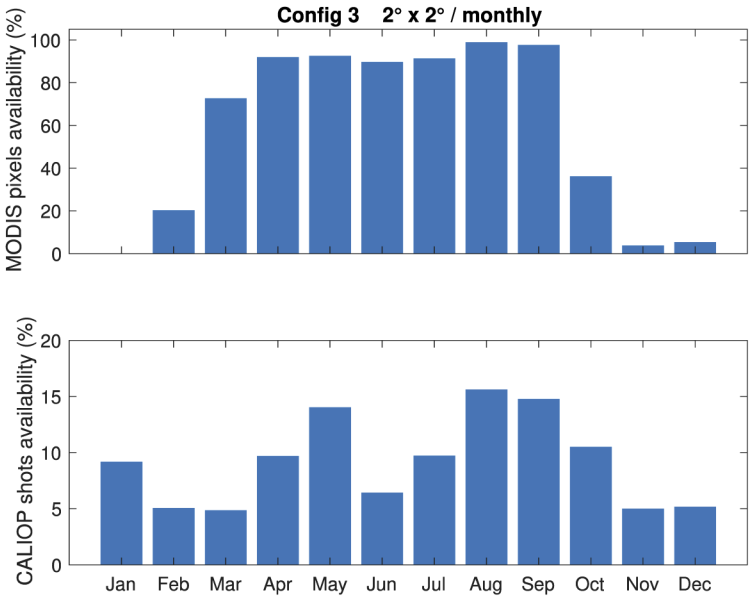

Fig. 2. Average percent of exploitable 9 by 9 km MODIS pixels (top) and CALIOP shots (bottom) within 2° by 2° degree boxes.

estimates were retrieved for 65% of the CALIOP shots at global scale in Behrenfeld et al. [3], we could only use 10% of total CALIOP shots (maximum of 17% in August, Fig. 2) in the North Atlantic subpolar ocean, using the same quality-control procedure. Indeed, when averaged over all boxes in August, 70% of the shots were above the column-integrated backscatter threshold (> 0.03 sr^{-1}) due to high cloud cover and aerosol loading, 23% were out of the wind speed limits, and 1% were flagged as bad quality data in level 1 products. After these filters were applied, another 85% of the shots were removed due to depolarization ratios δ_T>0.05. At this time and location, sea ice was absent, so a possible explanation of these high depolarization ratios is the low signal to noise ratio of the cross-polarization channel due to strong signal attenuation in the atmosphere. The same analysis was conducted (ConFig. 3), but using a column-integrated backscatter threshold of 0.017 sr^{-1} to insure perfectly clear and clean sky conditions [17]. This more restrictive threshold reduced the final percent of CALIOP shots used within each box (maximum of 13% in August) but allowed to select CALIOP profiles with potentially higher signal-to-noise ratio in subsurface layers. However, the average percent of CALIOP shots with depolarization ratio >0.05 remained high (minimum of 90% in August), suggesting that strong signal attenuation in the atmosphere cannot explain the high depolarization ratios observed. Daytime measurements in weakly scattering layers are strongly affected by the ambient solar background, which also causes a substantial deterioration of the signal-to-noise ratio [25]. Therefore, we conducted an additional analysis using only nighttime measurements. Again, the average percent of CALIOP shots with depolarization ratio >0.05 remained high (minimum of 80% in September), suggesting that low signal-to-noise ratio attributed to the ambient solar background cannot explain such high depolarization ratios.

The low proportion of good-quality CALIOP data was problematic when comparing b_{bp} estimates at fine spatio-temporal scales (i.e. ConFig. 1). Indeed, over 1002 possible matchups, b_{bp}^{CALIOP} estimates were retrieved for only 21 matchups. However, when CALIOP shots were binned at broader scales, the number of matchups (i.e. boxes with co-located CALIOP and float data) increased to 284 and 269 for ConFig. 2 and 3, respectively (Fig. 3). Figure 3 shows the

Optics EXPRESS

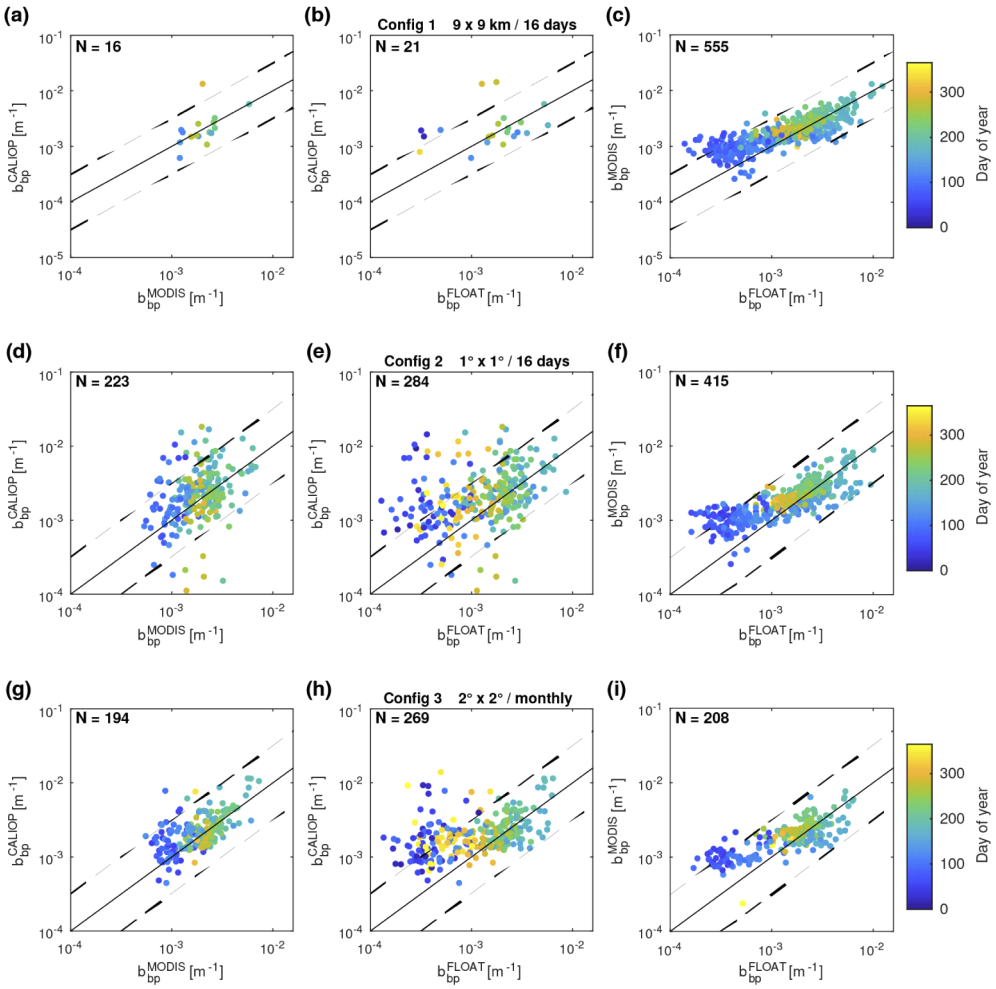

Fig. 3. Comparison of b_{bp} estimates from three different sources: CALIOP *vs.* MODIS (a, d, g), CALIOP *vs.* FLOAT (b, e, h), and MODIS *vs.* FLOAT (c, f, i). Three matchup configurations were tested: ConFig. 1 at 9 by 9 km and 16 days (a-c), ConFig. 2 at 1° by 1° and 16 days (d-f), ConFig. 3 at 2° by 2° and 1 month (g-i). Solid line represents perfect agreement, and dashed lines represent $\Delta = \pm 0.5$. Colors indicate the day of year.

comparisons between each pair of b_{bp} estimates from the three different sources. For ConFig. 1, the low number of matchups makes it difficult to assess the performances of CALIOP retrievals against MODIS data (Fig. 3(a)) or float data (Fig. 3(b)). However, the higher number of matchups between MODIS and float data (N = 555, Fig. 3(c)) clearly shows a good agreement between these two estimates. Table 2 provides the performance indices of b_{bp} estimates. The mean log-difference error between b_{bp}^{MODIS} and b_{bp}^{FLOAT} is $M_{(MODIS,FLOAT)} = 0.07$ with a correlation coefficient $r_{(MODIS,FLOAT)} = 0.82$, a root mean square relative error $RMS\%_{(MODIS,FLOAT)} = 8.05$ and a median ratio near unity ($F_{med}^{(MODIS,FLOAT)} = 1.17$, ConFig. 1). At broader scales (ConFig. 2), b_{bp}^{CALIOP} presents low correlation with both b_{bp}^{MODIS} ($r_{(MODIS,CALIOP)} = 0.35$, Fig. 3(d)) and b_{bp}^{FLOAT} ($r_{(FLOAT,CALIOP)} = 0.32$, Fig. 3(e)), and high RMS% values ($RMS\%_{(MODIS,CALIOP)} = 12.7$ and $RMS\%_{(FLOAT,CALIOP)} = 15.1$) compared to the float/MODIS relationship ($r_{(MODIS,FLOAT)} = 0.80$, $RMS\%_{(MODIS,FLOAT)} = 9.24$). At monthly and 2° by 2° grid resolution (ConFig. 3), b_{bp}^{CALIOP}

Optics EXPRESS

shows better agreement with both b_{bp}^{MODIS} and b_{bp}^{FLOAT}. Correlation coefficient increases to 0.61 with MODIS estimates and 0.44 with float estimates and RMS% values decreases significantly (RMS%$_{(MODIS,CALIOP)}$ = 7.12 and RMS%$_{(FLOAT,CALIOP)}$ = 13.2). b_{bp}^{CALIOP} slightly overestimates b_{bp}^{MODIS} and b_{bp}^{FLOAT} ($F_{med}^{(MODIS,CALIOP)}$ = 0.92 and $F_{med}^{(FLOAT,CALIOP)}$ = 0.58), especially for low b_{bp} values during winter months (Figs. 3(g)–(i)). Cumulative distribution functions in Fig. 4 clearly show this discrepancy for b_{bp} values $<1 * 10^{-3}$ (m^{-1}) which represent 10, 20 and 30% of the CALIOP, MODIS and floats dataset respectively. Biases in this range of values may be related to the inherent challenges of comparing data acquired with different instruments and associated detection limits. The limited number of data during winter months (Figs. 1 and 2) may also affect the signal to noise ratio within each box, as illustrated by the data dispersion in wintertime for ConFig. 2 and 3 (see Figs. 3(e) and (h)). It is worth noting that other configurations tested in clear sky conditions or during nighttime only did not allow improving the goodness of CALIOP estimates (Table 2).

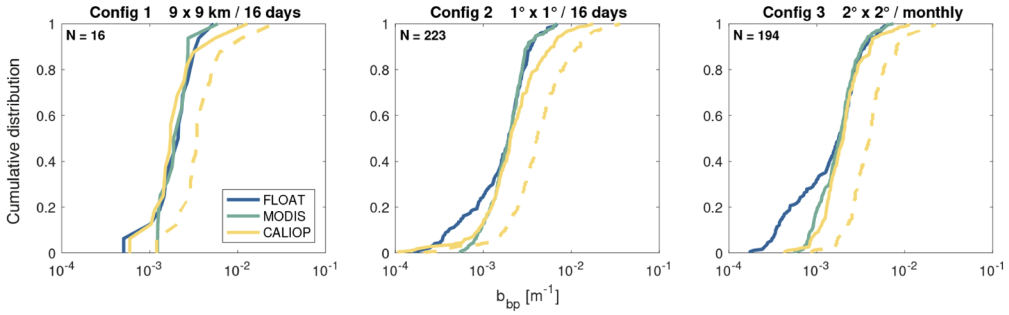

Fig. 4. Cumulative distribution of b_{bp} estimates from three different sources (FLOAT, CALIOP, MODIS) for ConFig. 1 (left), ConFig. 2 (middle) and ConFig. 3 (right). Only matchups with estimates from all sources were kept. The dashed yellow lines represent CALIOP estimates for a phase function $P_p(180, 532) = 0.16$, as in Behrenfeld et al. [3].

Figure 4 also shows the cumulative distribution functions of CALIOP estimates when the scattering phase function $P_p(\theta, \lambda)$ is set equal to 0.16, as in the global scale study of Behrenfeld et al. [3], instead of $P_p(\theta, \lambda) = 0.32$ as used in the present study and in Lu et al. [21]. In the North Atlantic, b_{bp}^{CALIOP} overestimates b_{bp}^{MODIS} and b_{bp}^{FLOAT} by a factor of 2 to 3 when $P_p(\theta, \lambda) = 0.16$. This demonstrates the need to adapt the scattering phase function at least regionally. Indeed, for $\theta > 150°$, $P_p(\theta, \lambda)$ exhibits high variability in natural waters with respect to optical properties and size distributions of suspended particles [26,27]. Other studies also reported the high variability of $P_p(\theta, \lambda)$ with respect to phytoplankton internal structure and shape [28,29], suggesting that seasonal changes in the phytoplankton community structure might affect the goodness of CALIOP estimates. However, despite the use of a constant value for $P_p(\theta, \lambda)$ and the strong spatio-temporal variability of b_{bp}^{FLOAT} estimates (nearly 2 orders of magnitude, Fig. 4), the reasonably good performance indices of the float/CALIOP relationship in Config 3 suggest that seasonal dynamics of particulate matter can be retrieved on basin scales. Dionisi et al. [6] also demonstrated that such seasonal dynamics can be retrieved from the CALIOP total column-integrated depolarization ratio δ_T, which has the advantage of being independent from $P_p(\theta, \lambda)$.

In this study, we chose to use the diffuse attenuation coefficient $K_d(532)$, derived from the floats (and not from MODIS), to compute CALIOP estimates, taking full advantage of the active sensor (CALIOP measurements day and night, throughout the year). Therefore, a dependency exists between CALIOP and float estimates, through $K_d(532)$. Figure 5 shows the relationship between b_{bp}^{FLOAT} and β_{w+}, the cross-polarized component of subsurface column-integrated backscatter, which is independent from $K_d(532)$. This relationship presents a similar correlation coefficient

Optics EXPRESS

Table 2. Performance indices based on log-difference errors Δ between b_{bp} estimates from three different sources (CALIOP, MODIS and FLOAT).[a]

	N	M	SD	RMS%	r	Fmed	Fmin	Fmax
MODIS *vs.* CALIOP								
$\Delta_{(MODIS,CALIOP)}$								
Config 1	16	0.009	0.26	9.2	0.54	1.02	0.56	1.85
Config 2	223	−0.05	0.35	12.7	0.35	0.88	0.39	1.96
Config 3	219	−0.04	0.19	7.12	0.61	0.92	0.58	1.46
FLOAT *vs.* CALIOP								
$\Delta_{(FLOAT,CALIOP)}$								
Config 1	21	−0.11	0.42	14.5	0.29	0.78	0.29	2.06
Config 2	284	−0.19	0.43	15.1	0.32	0.64	0.24	1.74
Config 3	275	−0.24	0.36	13.2	0.44	0.58	0.25	1.33
Config 3 clear sky	253	−0.20	0.36	12.9	0.44	0.62	0.27	1.42
Config 3 night time	183	−0.19	0.45	15.6	0.31	0.64	0.23	2.27
MODIS *vs.* FLOAT								
$\Delta_{(MODIS,FLOAT)}$								
Config 1	555	0.07	0.22	8.05	0.82	1.17	0.70	1.94
Config 2	415	0.11	0.24	9.24	0.80	1.28	0.73	2.23
Config 3	231	0.13	0.24	9.66	0.79	1.35	0.77	2.36

[a]N is the number of matchups. M and SD are the mean and standard deviation of log-difference errors and RMS% is the root mean square relative log-difference errors, respectively. r is the correlation coefficient. Median and one-sigma range of the ratio between b_{bp} estimates from different sources are given by F_{med}, F_{min} and F_{max}, respectively. Symbols Δ with subscripts refer to the notation in Eqs. (6)–(8).

(r = 0.38) to the one between b_{bp}^{FLOAT} and b_{bp}^{CALIOP}(r = 0.44), suggesting that the dependency mentioned earlier does not compromise the interpretation of our results.

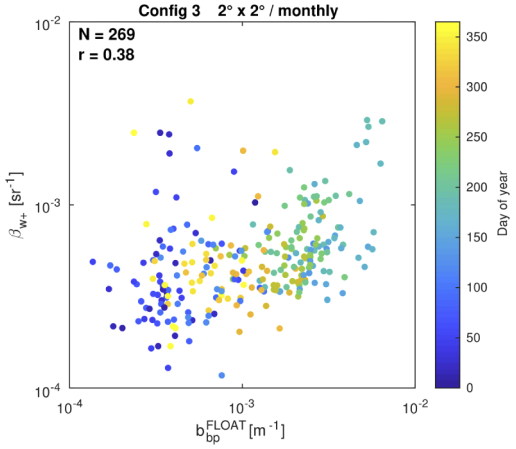

Fig. 5. Relationship between b_{bp}^{float} and the cross-polarized component of subsurface column-integrated backscatter (β_{w+}) derived from CALIOP. N is the number of matchups and r is the correlation coefficient.

Optics EXPRESS

4. Conclusion

The recent development of the BGC-Argo float network provided a new opportunity to evaluate CALIOP b_{bp} estimates over a complete annual cycle and on a basin scale. In the North Atlantic subpolar ocean, retrievals of good-quality CALIOP subsurface measurements were strongly constrained by the harsh weather conditions, thus drastically reducing the matchup possibilities at fine spatio-temporal scales. Therefore, we cannot conclude on the quality of CALIOP b_{bp} estimates at such scales. However, the low availability of these data reveals that any high-latitude oceanic applications at fine spatio-temporal scales would be highly challenging, if not impossible, with the present algorithm. At broader spatio-temporal scales, comparisons between CALIOP, MODIS and float estimates presented relatively good correlations, given the strong variability of year-round b_{bp} values in the study region. These results confirm the potential of spaceborne lidar for studying the seasonal dynamics of particulate matter on basin scales. We expect that the envisioned ocean-optimized satellite lidar will greatly improve b_{bp} estimates and extend the field of oceanic applications [30].

Funding

Centre National d'Etudes Spatiales; Canada First Research Excellence Fund; Canada Excellence Research Chairs, Government of Canada; European Research Council (GA 246777); Horizon 2020 Framework Programme (633211).

Acknowledgments

We thank the NASA Ocean Biology Processing Group for providing MODIS data, the joint CNES and NASA CALIPSO mission team for providing CALIOP data, and the International Argo Program and the CORIOLIS project for distributing BGC-Argo data.

Disclosures

The authors declare no conflicts of interest.

References

1. D. M. Winker, J. Pelon, J. A. Coakley, S. A. Ackerman, R. J. Charlson, P. R. Colarco, P. Flamant, Q. Fu, R. M. Hoff, C. Kittaka, T. L. Kubar, H. Le Treut, M. P. McCormick, G. Mégie, L. Poole, K. Powell, C. Trepte, M. A. Vaughan, B. A. Wielicki, D. M. Winker, J. Pelon, J. A. C. Jr, S. A. Ackerman, R. J. Charlson, P. R. Colarco, P. Flamant, Q. Fu, R. M. Hoff, C. Kittaka, T. L. Kubar, H. Le Treut, M. P. McCormick, G. Mégie, L. Poole, K. Powell, C. Trepte, M. A. Vaughan, and B. A. Wielicki, "The CALIPSO Mission: A Global 3D View of Aerosols and Clouds," Bull. Am. Meteorol. Soc. **91**(9), 1211–1230 (2010).
2. W. H. Hunt, D. M. Winker, M. A. Vaughan, K. A. Powell, P. L. Lucker, C. Weimer, W. H. Hunt, D. M. Winker, M. A. Vaughan, K. A. Powell, P. L. Lucker, and C. Weimer, "CALIPSO Lidar Description and Performance Assessment," J. Atmos. Ocean. Tech. **26**(7), 1214–1228 (2009).
3. M. J. Behrenfeld, Y. Hu, C. A. Hostetler, G. Dall'Olmo, S. D. Rodier, J. W. Hair, and C. R. Trepte, "Space-based lidar measurements of global ocean carbon stocks," Geophys. Res. Lett. **40**(16), 4355–4360 (2013).
4. X. Lu, Y. Hu, C. Trepte, S. Zeng, and J. H. Churnside, "Ocean subsurface studies with the CALIPSO spaceborne lidar," J. Geophys. Res. Oceans **119**(7), 4305–4317 (2014).
5. J. Churnside, B. McCarty, and X. Lu, "Subsurface Ocean Signals from an Orbiting Polarization Lidar," Remote Sens. **5**(7), 3457–3475 (2013).
6. D. Dionisi, V. E. Brando, G. Volpe, S. Colella, and R. Santoleri, "Seasonal distributions of ocean particulate optical properties from spaceborne lidar measurements in Mediterranean and Black sea," Remote Sens. Environ. **247**, 111889 (2020).
7. M. J. Behrenfeld, Y. Hu, R. T. O'Malley, E. S. Boss, C. A. Hostetler, D. A. Siegel, J. L. Sarmiento, J. Schulien, J. W. Hair, X. Lu, S. Rodier, and A. J. Scarino, "Annual boom-bust cycles of polar phytoplankton biomass revealed by space-based lidar," Nat. Geosci. **10**(2), 118–122 (2017).
8. L. Arteaga, N. Haëntjens, E. Boss, K. S. Johnson, and J. L. Sarmiento, "Assessment of Export Efficiency Equations in the Southern Ocean Applied to Satellite-Based Net Primary Production," J. Geophys. Res. Ocean **123**(4), 2945–2964 (2018).

Optics EXPRESS

9. C. A. Hostetler, M. J. Behrenfeld, Y. Hu, J. W. Hair, and J. A. Schulien, "Spaceborne Lidar in the Study of Marine Systems," Annu. Rev. Mar. Sci. **10**(1), 121–147 (2018).
10. C. Schmechtig, A. Poteau, H. Claustre, F. D'Ortenzio, G. Dall'Olmo, and E. Boss, *Processing Bio-Argo Particle Backscattering at the DAC Level* (Ifremer, 2018).
11. J. M. Sullivan, M. S. Twardowski, J. Ronald, V. Zaneveld, and C. C. Moore, "Measuring optical backscattering in water," in *Light Scattering Reviews 7: Radiative Transfer and Optical Properties of Atmosphere and Underlying Surface* (Springer Berlin Heidelberg, 2013), pp. 189–224.
12. E. Boss, M. Picheral, T. Leeuw, A. Chase, E. Karsenti, G. Gorsky, L. Taylor, W. Slade, J. Ras, and H. Claustre, "The characteristics of particulate absorption, scattering and attenuation coefficients in the surface ocean; Contribution of the Tara Oceans expedition," Methods Oceanogr. **7**, 52–62 (2013).
13. H. R. Gordon and D. K. Clark, "Remote sensing optical properties of a stratified ocean: an improved interpretation," Appl. Opt. **19**(20), 3428–3430 (1980).
14. N. Haëntjens, E. Boss, and L. D. Talley, "Revisiting Ocean Color algorithms for chlorophyll a and particulate organic carbon in the Southern Ocean using biogeochemical floats," J. Geophys. Res.: Oceans **122**(8), 6583–6593 (2017).
15. E. Organelli, H. Claustre, A. Bricaud, C. Schmechtig, A. Poteau, X. Xing, L. Prieur, F. D'Ortenzio, G. Dall'Olmo, and V. Vellucci, "A novel near-real-time quality-control procedure for radiometric profiles measured by bio-argo floats: Protocols and performances," J. Atmos. Ocean. Tech. **33**(5), 937–951 (2016).
16. E. Boss, D. Swift, L. Taylor, P. Brickley, R. Zaneveld, S. Riser, M. J. Perry, and P. G. Strutton, "Observations of Pigment and Particle Distributions in the Western North Atlantic from an Autonomous Float and Ocean Color Satellite," Limnol. Oceanogr. **53**(5part2), 2112–2122 (2008).
17. X. Lu, Y. Hu, J. Pelon, C. Trepte, K. Liu, S. Rodier, S. Zeng, P. Lucker, R. Verhappen, J. Wilson, C. Audouy, C. Ferrier, S. Haouchine, B. Hunt, and B. Getzewich, "Retrieval of ocean subsurface particulate backscattering coefficient from space-borne CALIOP lidar measurements," Opt. Express **24**(25), 29001–29008 (2016).
18. P. J. Werdell, B. A. Franz, S. W. Bailey, G. C. Feldman, E. Boss, V. E. Brando, M. Dowell, T. Hirata, S. J. Lavender, Z. Lee, H. Loisel, S. Maritorena, F. Mélin, T. S. Moore, T. J. Smyth, D. Antoine, E. Devred, O. H. F. d'Andon, and A. Mangin, "Generalized ocean color inversion model for retrieving marine inherent optical properties," Appl. Opt. **52**(10), 2019–2037 (2013).
19. D. M. Winker, M. A. Vaughan, A. Omar, Y. Hu, K. A. Powell, Z. Liu, W. H. Hunt, and S. A. Young, "Overview of the CALIPSO Mission and CALIOP Data Processing Algorithms," J. Atmos. Ocean. Tech. **26**(11), 2310–2323 (2009).
20. Y. Hu, K. Stamnes, M. Vaughan, J. Pelon, C. Weimer, D. Wu, M. Cisewski, W. Sun, P. Yang, B. Lin, A. Omar, D. Flittner, C. Hostetler, C. Trepte, D. Winker, G. Gibson, and M. Santa-Maria, "Sea surface wind speed estimation from space-based lidar measurements," Atmos. Chem. Phys. **8**(13), 3593–3601 (2008).
21. X. Lu, Y. Hu, Y. Yang, P. Bontempi, A. Omar, and R. Baize, "Antarctic spring ice-edge blooms observed from space by ICESat-2," Remote Sens. Environ. **245**, 111827 (2020).
22. M. J. Behrenfeld, Y. Hu, C. A. Hostetler, G. Dall'Olmo, S. D. Rodier, J. W. Hair, and C. R. Trepte, "Space-based lidar measurements of global ocean carbon stocks," Geophys. Res. Lett. **40**(16), 4355–4360 (2013).
23. J. Campbell, D. Antoine, R. Armstrong, K. Arrigo, W. Balch, R. Barber, M. Behrenfeld, R. Bidigare, J. Bishop, M.-E. Carr, W. Esaias, P. Falkowski, N. Hoepffner, R. Iverson, D. Kiefer, S. Lohrenz, J. Marra, A. Morel, J. Ryan, V. Vedernikov, K. Waters, C. Yentsch, and J. Yoder, "Comparison of algorithms for estimating ocean primary production from surface chlorophyll, temperature, and irradiance," Global Biogeochem. Cycles **16**(3), 1–15 (2002).
24. M. A. M. Friedrichs, M.-E. Carr, R. T. Barber, M. Scardi, D. Antoine, R. A. Armstrong, I. Asanuma, M. J. Behrenfeld, E. T. Buitenhuis, F. Chai, J. R. Christian, A. M. Ciotti, S. C. Doney, M. Dowell, J. Dunne, B. Gentili, W. Gregg, N. Hoepffner, J. Ishizaka, T. Kameda, I. Lima, J. Marra, F. Mélin, J. K. Moore, A. Morel, R. T. O'Malley, J. O'Reilly, V. S. Saba, M. Schmeltz, T. J. Smyth, J. Tjiputra, K. Waters, T. K. Westberry, and A. Winguth, "Assessing the uncertainties of model estimates of primary productivity in the tropical Pacific Ocean," J. Mar. Syst. **76**(1-2), 113–133 (2009).
25. K. A. Powell, C. A. Hostetler, M. A. Vaughan, K.-P. Lee, C. R. Trepte, R. R. Rogers, D. M. Winker, Z. Liu, R. E. Kuehn, W. H. Hunt, and S. A. Young, "CALIPSO Lidar Calibration Algorithms. Part I: Nighttime 532-nm Parallel Channel and 532-nm Perpendicular Channel," J. Atmos. Ocean. Tech. **26**(10), 2015–2033 (2009).
26. J. M. Sullivan and M. S. Twardowski, "Angular shape of the oceanic particulate volume scattering function in the backward direction," Appl. Opt. **48**(35), 6811–6819 (2009).
27. H. Tan, T. Oishi, A. Tanaka, and R. Doerffer, "Accurate estimation of the backscattering coefficient by light scattering at two backward angles," Appl. Opt. **54**(25), 7718–7733 (2015).
28. A. L. Whitmire, W. S. Pegau, L. Karp-Boss, E. Boss, and T. J. Cowles, "Spectral backscattering properties of marine phytoplankton cultures," Opt. Express **18**(14), 15073–15093 (2010).
29. T. Harmel, M. Hieronymi, W. Slade, R. Röttgers, F. Roullier, and M. Chami, "Laboratory experiments for inter-comparison of three volume scattering meters to measure angular scattering properties of hydrosols," Opt. Express **24**(2), A234–A256 (2016).
30. C. Jamet, A. Ibrahim, Z. Ahmad, F. Angelini, M. Babin, M. J. Behrenfeld, E. Boss, B. Cairns, J. Churnside, J. Chowdhary, A. B. Davis, D. Dionisi, L. Duforêt-Gaurier, B. Franz, R. Frouin, M. Gao, D. Gray, O. Hasekamp, X. He, C. Hostetler, O. V. Kalashnikova, K. Knobelspiesse, L. Lacour, H. Loisel, V. Martins, E. Rehm, L. Remer, I. Sanhaj, K. Stamnes, S. Stamnes, S. Victori, J. Werdell, and P.-W. Zhai, "Going Beyond Standard Ocean Color Observations: Lidar and Polarimetry," Front. Mar. Sci. **6**, 251 (2019).